

# First detection of $^{13}\text{CH}$ in the interstellar medium

Arshia M. Jacob<sup>1</sup>, Karl M. Menten<sup>1</sup>, Helmut Wiesemeyer<sup>1</sup>, Rolf Güsten<sup>1</sup>, Friedrich Wyrowski<sup>1</sup>, and Bernd Klein<sup>1,2</sup>

<sup>1</sup> Max-Planck-Institut für Radioastronomie, Auf dem Hügel 69, 53121 Bonn, Germany

<sup>2</sup> University of Applied Sciences Bonn-Rhein-Sieg, Grantham-Allee 20, 53757 Sankt Augustin, Germany  
e-mail: a.jacob@mpi.fr-bonn.mpg.de

Received September 15, 1996; accepted March 16, 1997

## ABSTRACT

In recent years, a plethora of high spectral resolution observations of sub-millimetre and far-infrared transitions of methyldene ( $\text{CH}$ ), conducted with Herschel and SOFIA, have demonstrated this radical to be a valuable proxy for molecular hydrogen, that can be used for characterising molecular gas within the interstellar medium on a Galactic scale, including the CO-dark component. Here we report the discovery of the  $^{13}\text{CH}$  isotopologue in the interstellar medium using the upGREAT receiver on board SOFIA. We have detected the three hyperfine structure components of the  $\approx 2$  THz frequency transition from its  $X^2\Pi_{1/2}$  ground-state toward the high-mass star-forming regions Sgr B2(M), G34.26+0.15, W49(N) and W51E and determine  $^{13}\text{CH}$  column densities. The ubiquity of molecules containing carbon in the interstellar medium has turned the determination of the ratio between the abundances of carbon's two stable isotopes,  $^{12}\text{C}/^{13}\text{C}$ , into a cornerstone for Galactic chemical evolution studies. Whilst displaying a rising gradient with Galactocentric distance, this ratio, when measured using observations of different molecules ( $\text{CO}$ ,  $\text{H}_2\text{CO}$ , and others) shows systematic variations depending on the tracer used. These observed inconsistencies may arise from optical depth effects, chemical fractionation or isotope-selective photo-dissociation. Formed from  $\text{C}^+$  either via UV-driven or turbulence-driven chemistry,  $\text{CH}$  reflects the fractionation of  $\text{C}^+$ , and does not show any significant fractionation effects unlike other molecules previously used to determine the  $^{12}\text{C}/^{13}\text{C}$  isotopic ratio which make it an ideal tracer for the  $^{12}\text{C}/^{13}\text{C}$  ratio throughout the Galaxy. Therefore, by comparing the derived column densities of  $^{13}\text{CH}$  with previously obtained SOFIA data of the corresponding transitions of the main isotopologue  $^{12}\text{CH}$ , we derive  $^{12}\text{C}/^{13}\text{C}$  isotopic ratios toward Sgr B2(M), G34.26+0.15, W49(N) and W51E. Adding our values derived from  $^{12/13}\text{CH}$  to previous calculations of the Galactic isotopic gradient we derive a revised value of  $^{12}\text{C}/^{13}\text{C} = 5.85(0.50)R_{\text{GC}} + 15.03(3.40)$ .

**Key words.** ISM: molecules – ISM: abundances – ISM: clouds – ISM: lines and bands – method: data analysis

## 1. Introduction

The methyldene radical,  $\text{CH}$  has received widespread attention as a general probe of diffuse and translucent interstellar clouds and in particular as a surrogate for the  $\text{H}_2$  column density determinations in such environments (e.g., Federman 1982; Sheffer et al. 2008, and references therein).  $\text{CH}$  has been observed in widely different wavelength regimes, from the radio at 9 cm (Rydbeck et al. 1973) over the sub-millimetre (sub-mm) and far-infrared (FIR) ranges, at 560  $\mu\text{m}$  (Gerin et al. 2010) and 150  $\mu\text{m}$  (Stacey et al. 1987; Wiesemeyer et al. 2018) and the optical (4300.3 Å. e.g., Danks et al. 1984; Sheffer et al. 2008) into the far-ultraviolet (FUV) regimes (1369.13 Å, Watson 2001). In fact, the famous 4300.3 Å  $\text{CH}$  transition was one of the first three molecular lines that were detected in the interstellar medium (ISM) (Dunham 1937; Swings & Rosenfeld 1937). While an abundance of  $^{12}\text{CH}$  data exists, very little is known about its rarer isotopologue  $^{13}\text{CH}$ . Unlike its parent molecule, which is ubiquitously distributed in the ISM, the only known astronomical identification of  $^{13}\text{CH}$  has been made in the solar spectrum by Richter & Tonner (1967). As to the ISM, Bottinelli et al. (2014) report the non-detection of the  $N, J = 1, 1/2 \rightarrow 1, 3/2$  and  $N, J = 1, 3/2 \rightarrow 2, 5/2$  transitions of  $^{13}\text{CH}$  toward the well studied low-mass protostellar condensation IRAS 16293–2422.

The  $^{12}\text{C}/^{13}\text{C}$  ratio has been widely studied toward molecular clouds in the Milky Way (e.g., Henkel et al. 1982; Steimle et al. 1986; Wilson & Rood 1994; Henkel et al. 1994) and,

recently, also in the nuclear regions of nearby starburst galaxies (Tang et al. 2019). It is an important diagnostic tool for probing Galactic chemical evolution or simply the nucleosynthesis history of the Galaxy.  $^{12}\text{C}$  is synthesised as the primary product of shell and core He-burning in intermediate- and high-mass stars via the triple- $\alpha$  reaction, while  $^{13}\text{C}$  is a secondary product of stellar nucleosynthesis and is produced over longer timescales. It is predominantly formed as a by-product of the carbon-nitrogen-oxygen (CNO) cycle in asymptotic giant branch (AGB) stars. Initiated by the proton capture of the  $^{12}\text{C}$  nucleus produced from an older stellar population, the CNO-cycle forms  $^{13}\text{N}$  which then decays via positron emission to form the  $^{13}\text{C}$  nucleus ( $^{12}\text{C}(p,\gamma)^{13}\text{N}(\beta^+)^{13}\text{C}$ ) (Pagel 1997). The  $^{13}\text{C}$  intermediate product is injected into the ISM via mass loss of the AGB stars, after the ashes of the helium burning shell of these objects have intermixed with their convective envelopes in the third “dredge-up” (Herwig 2005). This establishes the  $^{12}\text{C}/^{13}\text{C}$  isotopic ratio as a measure of the degree of astration present in the Galaxy. Chemical evolution models of the Galaxy (Tosi 1982; Prantzos et al. 1996) have predicted the  $^{12}\text{C}/^{13}\text{C}$  ratio to exhibit a positive gradient, increasing with Galactocentric distances and decreasing with time.

The predictions of these models have been confirmed by observational measurements of the  $^{12}\text{C}/^{13}\text{C}$  isotopic ratio carried out by studying the rotational transitions of molecules like  $\text{H}_2\text{CO}$  (Henkel et al. 1982),  $\text{CO}$  (Langer & Penzias 1990), and  $\text{CN}$  (Milam et al. 2005) and of their respective  $^{13}\text{C}$

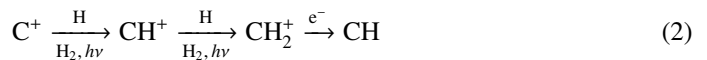
isotopologues, at cm and mm wavelengths<sup>1</sup>. While the average fit to the  $^{12}\text{C}/^{13}\text{C}$  gradients derived independently using the three molecules mentioned above are in agreement within the quoted error bars, their individual trends display systematic variations amongst themselves. Reasons for these variations may be related to the observations of the different tracers and/or to isotope-selective chemical processes like gas-phase fractionation and selective photo-dissociation which do not impact every molecule in the same way. Chemical fractionation occurs as a result of ion-molecule exchange reactions that preferentially transfer and incorporate the heavier atomic isotope into molecules due to differences in zero-point energies between the different isotopes (see, e.g., Wilson 1999; Roueff et al. 2015). Isotopic fractionation does not impact all molecules in the same way as its degree greatly depends upon the formation pathway of the molecule and the environment in which it is formed and exists. In molecules that are susceptible to fractionation, like CO, the chemical fractionation enriches the  $^{13}\text{C}$  isotope and lowers the  $^{12}\text{C}/^{13}\text{C}$  ratio while it is increased by selective photo-dissociation of the rarer isotopic species containing  $^{13}\text{C}$ , due to its weaker self-shielding in regions with a large UV flux (Bally & Langer 1982). Therefore, in such regions the  $^{12}\text{CO}/^{13}\text{CO}$  ratio might be higher than the underlying  $^{12}\text{C}/^{13}\text{C}$  ratio. In denser regions where carbon exists mostly in the form of CO,  $^{13}\text{C}$  is locked up in CO and is depleted in other carbon-bearing molecules (Roueff et al. 2015). Precise measurements of the  $^{12}\text{C}/^{13}\text{C}$  isotopic ratio have also been made using observations of the  $\text{CH}^+ A - X (0, 0)$  transition near 4232 Å (Ritchey et al. 2011) but their observations are limited to nearby stars (<7 kpc) that are bright ( $V < 10$  mag) in the visible wavelength range. The corresponding sub-mm transitions of  $\text{CH}^+$  are often optically thick with saturated absorption profiles and can only yield lower limits on the carbon isotopic ratio (Falgaroni et al. 2010). Hence, the high optical depths of many abundant  $^{12}\text{C}$  bearing molecules, and effects of saturation and self absorption pose a problem when using the intensities of such lines, which in turn skews estimates of the  $^{12}\text{C}/^{13}\text{C}$  ratio. In an attempt to provide additional constraints on the  $^{12}\text{C}/^{13}\text{C}$  ratio, we here propose the use of a new tracer – CH.

CH should be a good candidate for conducting isotopic ratio measures because it is an abundant species that is ubiquitously formed in the ISM and its spectral lines are predominantly optically thin. In particular, the hyperfine structure (hfs) components of the  $N, J = 1, 1/2 \rightarrow 2, 3/2$  transitions of CH near 2 THz have recently been observed in generally unsaturated absorption, ideal for column density determinations (Wiesemeyer et al. 2018; Jacob et al. 2019). Models and simulations by Röllig & Ossenkopf (2013) for photo-dissociation regions (PDRs) show that the fractionation present in CH is dominated by the fractionation of its parental species. CH originates from  $\text{C}^+$  and is formed via the dissociative recombination of  $\text{CH}_3^+$ :



Hence, the degree of fractionation in CH is closely coupled with that of  $\text{C}^+$ . At low visual extinctions,  $A_V$ , the isotopic fractionation ratio of  $\text{C}^{+2}$  is comparable to the elemental abundance ratio, however, it increases with  $A_V$  at low gas

temperatures typically by a factor of at most  $\sim 2$ . This is a consequence of the enrichment of  $^{13}\text{C}$  in CO in these regions (favouring the forward reaction of the  $\text{C}^+ - \text{CO}$  ion-molecule exchange reaction (Langer & Penzias 1990)), which results in the depletion of  $^{13}\text{C}^+$  and all subsequent species like  $^{13}\text{CH}$  that are formed from it. In addition, the abundance of CH is often enhanced through hydrogen abstraction reactions of  $\text{CH}^+$ , which is formed endothermically ( $\Delta E/k_B = 4620$  K) (Hierl et al. 1997), in shocks or the dissipation of turbulence (Godard et al. 2014), followed by the dissociative recombination of  $\text{CH}_2^+$ :



Being formed at high effective temperatures via non-thermal processes,  $\text{CH}^+$  is not affected by fractionation and is believed to reflect the ambient C-isotopic ratio in the diffuse ISM. Hence, in low  $A_V$  diffuse clouds, where turbulence driven reactions are favoured, CH, like its parent  $\text{CH}^+$ , is not affected by fractionation. Therefore, the abundance ratio of the CH isotopologues does not deviate from the elemental ratio of the atomic carbon isotopes.

As mentioned above, optical and UV absorption studies of CH require visually bright early type stars as background whose light is unhampered by interstellar extinction (Federman 1982; Sheffer et al. 2008). Owing to this, they can only probe the ISM in the solar neighbourhood out to a few kpc. In contrast, we observe supra-THz transitions of CH and  $^{13}\text{CH}$  in absorption against the bright dust emission of far away star-forming regions (SFRs) out to the Galactic centre (GC) and beyond. Thus our absorption spectra not only probe the molecular envelopes of these sources, but also the diffuse and translucent interstellar clouds along their lines of sight over a wide range of Galactocentric radii. Due to the Galaxy's differential rotation, the absorption covers wide local standard of rest (LSR) velocity ranges. As a caveat, we mention that given, first, the expected  $^{12}\text{CH}/^{13}\text{CH}$  ratios, which range from  $\approx 20$  in the GC to  $\approx 90$  at the Solar circle and even higher values beyond (Wilson & Rood 1994, and references therein) and, second, that even  $^{12}\text{CH}$  lines are predominantly optically thin<sup>3</sup> we expect a detection of  $^{13}\text{CH}$  absorption only toward the LSR velocities of the star forming regions studied, because these sources have far greater column densities than the intervening diffuse clouds along their lines of sight. In this paper, we present our search for  $^{13}\text{CH}$  in the ISM along the line-of-sight (LOS) toward five high-mass SFRs in the Milky Way, Sgr B2(M), G34.26+0.15, W49(N), W51E and W3(OH) and discuss its use as an unbiased tool for benchmarking the  $^{12}\text{C}/^{13}\text{C}$  Galactic gradient.

## 2. $^{13}\text{CH}$ spectroscopy

Similar to CH,  $^{13}\text{CH}$  conforms to Hund's case b coupling but differs in the nuclear spin,  $I$ , of the Carbon atom,  $I(^{12}\text{C})=0$  and  $I(^{13}\text{C})=0.5$ . Due to the non-zero nuclear spin of the  $^{13}\text{C}$  isotope, the total angular momentum  $J$  first couples with  $I_1(^{13}\text{C})$  to generate  $F_1 (= J + I_1)$  which further couples with the nuclear spin of the H atom,  $I_2(\text{H}) = 0.5$  to yield  $F (= F_1 + I_2)$ . The energy level diagram of the  $^{13}\text{CH}$   $\Lambda$ -doublet transitions that are discussed in this study are displayed in Fig. 1. Considerable

<sup>1</sup> Where the lines from the isotopologues are well separated unlike in the optical regime (except for  $^{12/13}\text{CH}^+$  see, Ritchey et al. (2011)).

<sup>2</sup> Ossenkopf et al. (2013) have studied the fractionation of  $\text{C}^+$  by comparing model predictions with high-resolution observations of the fine structure lines of  $^{12}\text{CII}$  and  $^{13}\text{CII}$  using HIFI/Herschel.

<sup>3</sup> Quite remarkably, this is actually generally true for radio, sub-mm, FIR and optical CH lines, except for the ground state rotational sub-mm/FIR transitions near 533/536, and 2006/2010 GHz, which reach optical depths exceeding unity in absorption from the envelopes of star forming regions; see, e.g., our Fig.2.

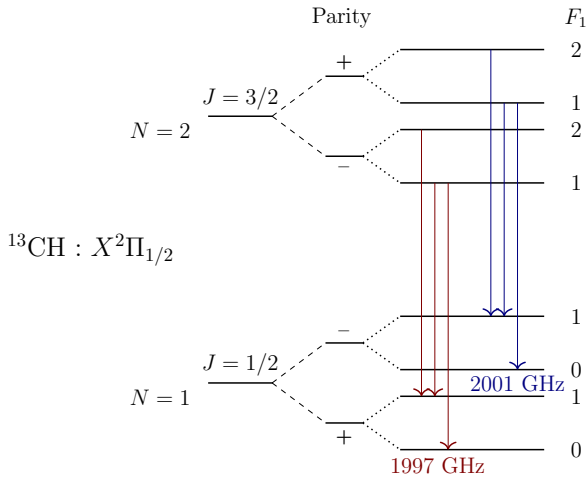


**Fig. 1.** Energy-level diagram of the lower rotational levels of  $^{13}\text{CH}$ . The hyperfine transitions of  $^{13}\text{CH}$  that are presented in this study are highlighted using red and blue arrows. The proton hyperfine structure splittings are not included. Note that the level separations are not to scale.

**Table 1.** Spectroscopic parameters for the  $N, J = 2, 3/2 \rightarrow 1, 1/2$  hyperfine structure transitions of  $^{13}\text{CH}$ . Taken from Davidson et al. (2004).

Parity	Transition	Frequency [GHz]	$S$	$A_E \times 10^{-3}$ [s $^{-1}$ ]
$+\rightarrow-$	$1, 3/2 \rightarrow 0, 1/2$	1997.4232	0.3331	1.1458
	$1, 3/2 \rightarrow 1, 3/2$	1997.4464	0.1666	0.5731
	$2, 5/2 \rightarrow 1, 3/2$	1997.4437	0.8327	1.9096
$-\rightarrow+$	$1, 3/2 \rightarrow 0, 1/2$	2001.5672	0.3345	1.1577
	$1, 3/2 \rightarrow 1, 3/2$	2001.2230	0.1673	0.5787
	$2, 5/2 \rightarrow 1, 3/2$	2001.3673	0.8365	1.9296

effort has been expended in the laboratory to measure the rotational spectrum of  $^{13}\text{CH}$ . The spectroscopic parameters of the rotational transitions of the  $^{13}\text{CH}$  radical between the  $X^2\Pi$  ground state have been measured using the technique of laser magnetic resonance (LMR) at FIR wavelengths by Davidson et al. (2004). The results of their experiments were combined with previously determined  $\Lambda$ -doublet intervals of the molecule by Steimle et al. (1986) to provide accurate predictions of the transition frequencies between the low-lying rotational levels and the ground state. The spectroscopic parameters of the observed  $N, J = 2, 3/2 \rightarrow 1, 1/2$  transitions are tabulated in Table 1. The Einstein A coefficients,  $A_{E,ij}$ , were computed from the line strengths,  $S_{ij}$ , using the relation:

$$A_{E,ij} = (16\pi^3 \nu_{ij}^3 / 3\epsilon_0 h c^3) (2F_i + 1)^{-1} S_{ij} \mu^2 \quad (3)$$

for spontaneous emission from an energy level  $i$  to  $j$ . Where  $\nu_{ij}$  is the corresponding frequency,  $F_i$  is the total hyperfine quantum number, of level  $i$  and  $\mu$  represents the electric dipole moment of  $^{13}\text{CH}$ ,  $\mu(^{13}\text{CH}) = 1.46$  Debye (Pickett et al. 1998).

### 3. Observations

Using the upGREAT instrument<sup>4</sup> (Risacher et al. 2016) on board SOFIA (Young et al. 2012), we observed the  $^2\Pi_{1/2} N, J = 2, 3/2 \rightarrow 1, 1/2$   $\Lambda$ -doublet transitions of  $^{13}\text{CH}$  over several flight series as a part of the observatory’s cycle 7 campaign (under the open time project 07\_0148 supplemented by guaranteed time observations). In this pilot study we carried out observations toward five well known SFRs Sgr B2(M), G34.26+0.15, W49(N), W51E, and W3(OH). Given that so far  $^{13}\text{CH}$  has never been detected in the ISM before, the primary source selection criterion was the existence of a strong sub-mm and FIR background continuum. Secondly, we selected sources that are almost evenly spaced in Galactocentric distance between the GC and the Solar circle in order to obtain quantitative constraints on the Galactic  $^{12}\text{C}/^{13}\text{C}$  abundance ratio gradient. Observational properties of the different sources are summarised in Tab. 2. The receiver configuration is comprised of the (7+7) pixel low frequency array (LFA) receiver module of upGREAT, in dual polarisation. Only data from the central pixels were used because the continuum targets are unresolved in our 13.5'' FWHM beam<sup>5</sup>. The spectra were taken in the double-beam switch mode, chopping at a frequency of 2.5 Hz with a chop throw between 210'' and 240'' and a chop angle of 90° (counter-clockwise against North), to account for both atmospheric fluctuations, as well as fluctuations that may arise from the instrument. The receiver was connected to an evolved version of the MPIfR Fast Fourier Transform Spectrometer described by Klein et al. (2012). This backend provides a 4 GHz bandwidth per pixel and a velocity resolution of 0.036 km s $^{-1}$  ( $\sim 244.1$  kHz) over 16384 channels. In this detection experiment, the double-sideband (DSB) receiver was tuned to 1997.4437 GHz (the strongest hfs transition of the 1997 GHz  $\Lambda$ -doublet) in the lower sideband. Three different intermediate-frequency (IF) settings were used in our observations in order to disentangle any contamination present in the bandpass, toward all sources except W3(OH) toward which we used only a single IF setting at 1.45 GHz in our pilot search. For G34.26+0.15, W49(N) and W51E the IF was tuned to 1.2, 1.4 and 1.6 GHz while for Sgr B2(M) the IF was tuned to 1.4, 1.6, and 1.8 GHz. The  $^{13}\text{CH}$  spectra obtained along the LOSs to Sgr B2(M), G34.26+0.15, W51E and W49(N) taken with each of the three IF settings are displayed in Appendix. A. Using a forward efficiency of 0.97 the spectra were further calibrated using the KALIBRATE program (Guan et al. 2012). Fluctuations of the continuum level can either be due to telescope tracking problems, or due to gain drifts in the mixers. From a comparison between the continuum fluxes in the high-frequency array, operated in parallel at 4.7 THz and offering a 6'' FWHM beam, we can rule out the former (which even if they occurred would not have an impact on the line-to-continuum ratio). Gain drifts that are faster than the calibration rate, however, affect the measurement of the atmospheric total power and therefore the applied transmission correction. Since they potentially distort the line-to-continuum ratio, a new calibration strategy was applied to analyse the gain fluctuations of the GREAT receiver, thanks to the larger amount of data now available. In a first step, the most stable off-centre pixels were identified by monitoring the line areas of a simultaneously

<sup>4</sup> The German REceiver for Astronomy at Terahertz frequencies (GREAT) is a development by the MPI für Radioastronomie and the KOSMA/Universität zu Köln, in cooperation with the DLR Institut für Optische Sensorsysteme.

<sup>5</sup> The beam-size is scaled with frequency from the nominal 14.1'' beam width at the [CII] 158  $\mu\text{m}$  line.

**Table 2.** Continuum source parameters.

Source	$\alpha$ (J2000) [h:m:s]	$\delta$ (J2000) [° :′ :″]	$v_{\text{LSR}}$ [kms <sup>-1</sup> ]	$T_c$ [K]	$R_{\text{GC}}$ [kpc]	$D$ [kpc]	Flight Id	$t_{\text{obs}}^a$ [mins]
Sgr B2(M)	17:47:20.49	-28:23:06.00	65.2(0.6)	14.6	0.1	8.3	2019/06/10(F579)	51
							2019/06/11(F580)	101
W51E	19:23:43.90	+14:30:30.50	63.0(1.6)	9.4	6.3	5.4	2019/12/11(F646)	90
G34.26+0.15	18:53:18.49	+01:14:58.70	58.0(0.7)	8.6	7.0	1.6	2020/03/07(F669)	126
							2020/03/11(F671)	85
W49(N)	19:10:13.20	+09:06:11.88	11.8(0.4)	13.8	7.8	11.4	2020/03/05(F667)	80
							2020/03/10(F670)	55
							2020/03/12(F673)	135
							2020/03/13(F674)	57
W3(OH)	02:27:04.10	+61:52:22.00	-46.0(0.2)	5.3	10.0	2.0	2018/11/21(F529)	117
							2018/12/04(F533)	53

**Notes.** Columns are, left to right, source designation, equatorial coordinates, LSR velocity, signal band continuum brightness temperature derived by means of a DSB calibration, Galactocentric distance, heliocentric distance, flight id and flight leg duration. <sup>(a)</sup> The observing leg time ( $t_{\text{obs}}$ ) refers to the total duration of time for which the source was observed. This includes the total (on+off) observing time as well as the overheads, which in total is typically a factor of two larger than the (on+off) time.

**References.** References for the heliocentric distances: Sgr B2(M): Reid et al. (2014); W51E: Sato et al. (2010); G34.26+0.15: Zhang et al. (2009); W49(N): Zhang et al. (2013); W3(OH): Xu et al. (2006);

observed narrow telluric ozone line, which is largely insensitive to baseline uncertainties. Since the atmospheric emission arises in the near-field of all pixels, they must, therefore, all see the same ozone line flux. From this correlation analysis, only those pixel pairs whose line flux ratios were persistently close to unity were retained to determine the atmospheric transmission correction. The quality of the correlation analysis was ensured by forming closure products of the gain ratios, including those of the central pixel used (which for our case deviates from unity by at most 1.6%). In order to eliminate spectra in the central pixel affected by gain drifts, only data with closure products deviating from unity by at most 0.4% were retained to determine the continuum level. The DSB-continuum level is then determined by accounting for contributions from both the signal and image bands, which is added back to the spectra to obtain the correct line-to-continuum ratio. This calibration technique was applied not only to the <sup>13</sup>CH data presented in this work but also to the previously published <sup>12</sup>CH data (Wiesemeyer et al. 2018; Jacob et al. 2019), which thus were re-calibrated for use in our analysis, to avoid any inconsistencies. For the <sup>12</sup>CH spectra, we note that the continuum levels derived using the closure products are compatible with those derived using the standard calibration methods, except for W49(N). Using the closure product analysis we derive a continuum level of 14 K for the <sup>12</sup>CH spectrum toward W49(N) which agrees with the continuum level cited by Wiesemeyer et al. (2018) within a 20% uncertainty. It is to be noted that, in the analysis that follows, we adopt a value of 14 K as the continuum level of the <sup>12</sup>CH spectrum toward W49(N).

Subsequently, the fully calibrated spectra obtained from both polarisations of the central pixel were converted to main-beam brightness temperature scale (using a main beam efficiency of 0.66) and analysed using the GILDAS-CLASS software<sup>6</sup>. The spectra were box-smoothed to  $\sim 1.1$  km s<sup>-1</sup> wide velocity bins and the spectral baselines were corrected for by removing up to a second order polynomial. The resultant spectra obtained after carrying out a simple sideband deconvolution (discussed in Appendix A) are displayed in Figures 2 and 3. On average

<sup>6</sup> Software package developed by IRAM, see <https://www.iram.fr/IRAMFR/GILDAS/> for more information regarding GILDAS packages.

we achieved a noise level of  $\sim 68$  mK at a velocity resolution of 1.1 km s<sup>-1</sup> after the sideband deconvolution. In the following paragraphs we briefly describe the LOS properties of the observed <sup>13</sup>CH spectra and compare them with previously obtained CH spectra.

Sgr B2(M): The unwavering nature of the absorption feature at  $\nu \sim 64$  km s<sup>-1</sup> observed toward the envelope of Sgr B2(M) in each of the different IF frequency settings and the detection of its image band  $\Lambda$ -doublet counterpart near 2001 GHz with the absorption features displaying their expected relative intensities, solidifies our detection of <sup>13</sup>CH near 1997.44 GHz at this velocity. We compare the <sup>13</sup>CH spectrum with that of CH towards Sgr B2(M) published in Jacob et al. (2019). The CH spectrum has a true continuum of 15 K and is contaminated by C<sub>3</sub> absorption at 2004.833 GHz arising from the image band as indicated by the blue box in Fig. 2. The similarities between the CH and <sup>13</sup>CH spectra suggest the presence of weak blue-shifted sight-line absorption features in addition to the deep absorption seen near 64 km s<sup>-1</sup> corresponding to the systemic LSR velocity of the molecular cloud. The shift of the atmospheric ozone feature at 2002.347 GHz in the image band toward the signal band features, by 60 km s<sup>-1</sup> with each 0.2 GHz IF offset, leads to uncertainties while fitting polynomial baselines particularly for the weaker features. Hence, the true nature of the sight-line absorption features remains uncertain because of calibration and baseline uncertainties for the broad blended features. We will follow this up in future observations.

G34.26+0.15: In order to avoid the blending of the atmospheric ozone feature from the image band with the signal band features, we used an IF setting of 1.2 GHz instead of 1.8 GHz. Similar to the <sup>13</sup>CH spectrum observed toward Sgr B2(M), we see absorption at the systemic velocity of the G34.26+0.15 molecular cloud at 58 km s<sup>-1</sup>, in all three IF settings. However, we do not clearly detect <sup>13</sup>CH in foreground gas at velocities between 0 and 50 km s<sup>-1</sup>.

W49(N): We used a setup similar to that used for our observations toward G34.26+0.15 for those toward W49(N). In addition to <sup>13</sup>CH absorption at the velocities corresponding to that of the molecular cloud, we see a weaker absorption feature close to 65 km s<sup>-1</sup>, associated with the far-side crossing of the

Sagittarius spiral arm. However, we do not include this feature in the analysis that follows because of its low signal-to-noise level.

W51E: By choosing the 1.4 GHz IF tuning as the nominal setting for carrying out the DSB deconvolution, we observe  $^{13}\text{CH}$  absorption at the source intrinsic velocity of W51E near  $\sim 62 \text{ km s}^{-1}$ . Comparing this with the corresponding  $^{12}\text{CH}$  spectrum which closely resembles that of the  $^2\Pi_{3/2}, J = 3/2 \rightarrow 5/2$  SH line at 1383.2 GHz, between 43–80  $\text{km s}^{-1}$  (Neufeld et al. 2015), it is not clear whether  $^{13}\text{CH}$  shows a second absorption component at  $53 \text{ km s}^{-1}$  at the given noise level. The weaker and narrower absorption seen at  $26 \text{ km s}^{-1}$  is merely a remnant feature from the image band.

Toward W3(OH) no  $^{13}\text{CH}$  lines are detected above the noise (77 mK at a spectral resolution of  $1.1 \text{ km s}^{-1}$ ) in the spectrum at a continuum level of 5.3 K. The baseline-subtracted CH and  $^{13}\text{CH}$  spectra toward W3(OH) are displayed in Appendix B.1. The corresponding CH spectrum is taken from Wiesemeyer et al. (2018) and has a continuum level at 5.4 K, prior to baseline removal.

Additionally we have checked whether the  $^{12}\text{C}/^{13}\text{C}$  ratios derived by us are consistent with values derived using archival HIFI/Herschel data of the  $N, J = 1, 3/2 \rightarrow 1, 1/2$  transitions of CH and  $^{13}\text{CH}$  near 532 GHz. While the 532 GHz CH line displays a deep absorption feature at the systemic velocity of the Sgr B2(M) molecular cloud with a peak temperature of 1.64 K (Qin et al. 2010), the corresponding  $^{13}\text{CH}$  transition is not detected above a  $3\sigma$  noise level of 0.33 K (at a spectral resolution of  $0.5 \text{ km s}^{-1}$ ) and yields a lower limit of 5 on the  $^{12}\text{C}/^{13}\text{C}$  isotopic ratio. Similarly, we have analysed the 532 GHz CH spectra taken toward G34.26+0.15 discussed in Godard et al. (2012), W49(N), and W51E presented in Gerin et al. (2010) and W3(OH) from the Herschel archives<sup>7</sup> that also cover the corresponding  $^{13}\text{CH}$  line frequencies. We find no signatures of  $^{13}\text{CH}$  and, from the  $3\sigma$  noise levels, are only able to derive lower limits to the  $^{12}\text{C}/^{13}\text{C}$  ratio of 13, 32, 17, 68 for the above sources. We mention that, in contrast to the 2 THz lines, in the 532 GHz line, the molecular cores associated with these massive SFRs show complex line profiles with both emission and absorption components. In addition, the intensities and profiles of the  $^{13}\text{CH}$  lines are quite uncertain as their HIFI spectra are affected by a standing wave and an unknown (and not yet assessed) level of potential line contamination. Thus the formal lower limits for the  $^{12}\text{C}/^{13}\text{C}$  ratio derived from archival HIFI/Herschel data quoted above should be regarded with some caution.

#### 4. Analysis and Discussion

High-resolution absorption line spectroscopy provides a powerful and straightforward to use tool for measuring column densities. The optical depth,  $\tau$ , for a single absorption component can be calculated from the line to continuum ratio using

$$\tau = -\ln(T_l/T_c), \quad (4)$$

where  $T_l$  and  $T_c$  represent the observed brightness temperatures of the line (prior to continuum subtraction) and the continuum, respectively. We have determined the optical depth profile, i.e.,  $\tau$  vs.  $v_{\text{LSR}}$ , using the Wiener filter fitting technique as described in Jacob et al. (2019). This fitting procedure first, fits the observed spectral profile by minimising the mean square error between the model and observations and then deconvolves the hyperfine structure from the observed spectrum using the hfs components<sup>7</sup>

relative weights. Other than the observed spectrum and the spectroscopic parameters of the line to be fit, the only other input parameter required by the Wiener filter technique is the spectral noise, which is assumed to be independent of the observed signal. The resulting deconvolved optical depth signature,  $\tau_{\text{decon}}$ , can then be converted into column density values per velocity channel,  $i$  using

$$\left(\frac{dN}{dv}\right)_i = \frac{8\pi\nu_i^3}{c^3} \frac{Q_{\text{rot}}}{g_u A_E} \exp\left(\frac{E_u}{T_{\text{ex}}}\right) \left[ \exp\left(\frac{h\nu_i}{k_B T_{\text{ex}}}\right) - 1 \right]^{-1} (\tau_{\text{decon}})_i, \quad (5)$$

where the spectroscopic parameters  $g_u$  (the upper level degeneracy),  $E_u$  (the upper level energy) and  $A_E$  (the Einstein A coefficient) remain constant for a given hyperfine transition. The partition function,  $Q$  is itself a function of the rotation temperature,  $T_{\text{rot}}$ , which would be equal to the excitation temperature,  $T_{\text{ex}}$ , under conditions of local thermodynamic equilibrium (LTE). Typically the rotational transitions of hydrides require large critical densities to be observable in emission. Since collisional rate coefficients are not presently available for  $^{13}\text{CH}$ , we assume the critical density of this  $^{13}\text{CH}$  line to be identical to the critical density of the corresponding CH transition, assuming a two-level system. Using hfs resolved collisional rate coefficients computed by Dagdigan (2018), we find the critical densities to be  $\sim 2 \times 10^9 \text{ cm}^{-3}$  at 50–100 K. Within the diffuse and translucent interstellar clouds along the LOS ( $n = 10 - 500 \text{ cm}^{-3}$ ) and the envelope of Sgr B2(M) (ranging from  $n \sim 10^3 - 10^5 \text{ cm}^{-3}$ ; (Schmiedeke et al. 2016)) the gas densities are much lower than the critical density,  $n_{\text{crit}}$ , of these transitions making them sub-thermally excited. Hence we can assume the excitation temperature of such sub-thermally excited lines to be small and lower than the gas kinetic temperature. In our analysis we assume  $T_{\text{rot}}$  to be equal to the temperature of the cosmic microwave background (CMB) radiation,  $T_{\text{CMB}} = 2.728 \text{ K}$  (Neill et al. 2014). Given this low rotation temperature and the inefficacy of purely collisional excitation, almost all of the CH molecules will reside in the molecule's ground state level. However, in the SFRs, radiative excitation by FIR dust radiation can affect the level populations (see, Neufeld et al. (1997) for the case of HF). Meaningful modelling of this is beyond the scope of the present study. In any case, given that the  $^{12}\text{CH}$  and  $^{13}\text{CH}$  lines under consideration here have, respectively, moderate and low optical depths, radiative excitation is expected to affect the observed transitions from both isotopologues in a similar way, leaving the  $^{12}\text{CH}/^{13}\text{CH}$  intensity ratio unaltered.

Given the knowledge of the frequency separation of the hfs transitions of  $^{13}\text{CH}$ , we first deconvolve the hyperfine structure from the observed spectra using the Wiener filter formalism (briefly discussed above) and then derive column densities by adopting a  $T_{\text{ex}}$  value equal to  $T_{\text{CMB}}$  and integrating over the deconvolved velocity range of the line. We derive  $^{13}\text{CH}$  column densities between  $\sim 2 \times 10^{12}$  and  $4.6 \times 10^{13} \text{ cm}^{-2}$  toward the different sources. Given that the optical depths are computed directly from the line-to-continuum ratio, the uncertainties in the true continuum level give rise to systemic errors in the derived column densities. We assume a 10% error in the continuum level calibration based on the instrumental performance (Kester et al. 2017) and sideband dependence of the atmospheric transmission. The subsequently derived errors in the column densities (per velocity interval) are computed following the description presented in Jacob et al. (2019) and scale with the deconvolved optical depths by a constant term comprised of the spectroscopic parameters that govern the transition and the

<sup>7</sup> See, <http://archives.esac.esa.int/hsa/whsa/>

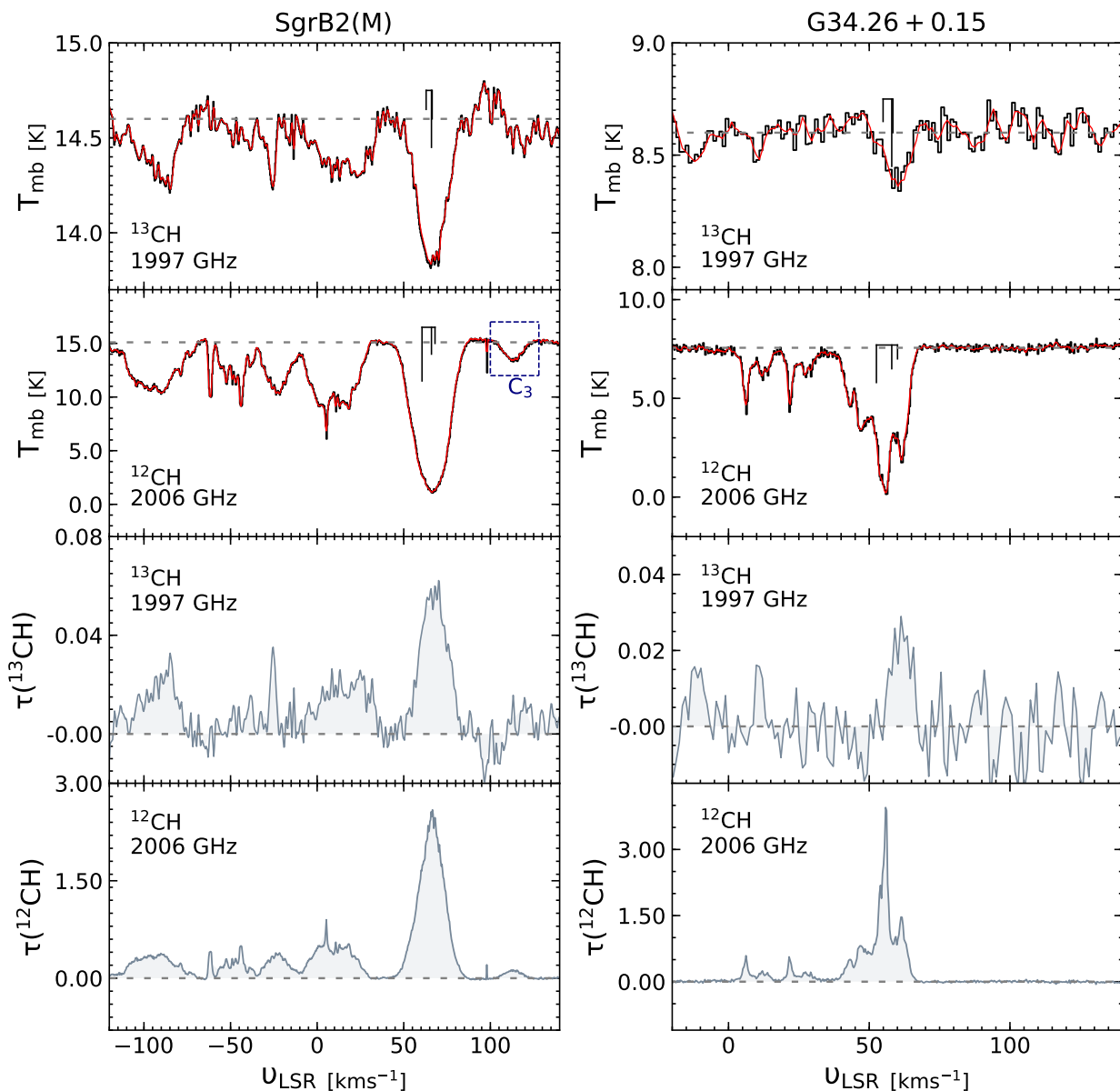


**Fig. 2.** From top to bottom:  $N, J = 2, 3/2 \rightarrow 1, 1/2$  transition spectra of  $^{13}\text{CH}$  and  $\text{CH}$  near 1997 GHz and 2006 GHz, in black with their corresponding Wiener filter fits to the spectra overlaid in red toward Sgr B2(M) (left) and G34.26+0.15 (right). Followed by their Wiener filter deconvolved spectra displayed in grey in optical depth scales. Note: The  $^{12}\text{CH}$  spectrum toward Sgr B2(M) is contaminated by  $\text{C}_3$  absorption at 2004.833 GHz in the image band as indicated in blue.

excitation temperature. We compare the  $^{13}\text{CH}$  column densities derived here, over velocity intervals associated with the different molecular clouds, with those of their corresponding  $N, J = 2, 3/2 \rightarrow 1, 1/2$  hyperfine hfs transitions of  $\text{CH}$  near 2007 GHz discussed in Wiesemeyer et al. (2018) and Jacob et al. (2019). In Tab. 3, we present the derived  $^{12}\text{CH}$  and  $^{13}\text{CH}$  column densities, using the same excitation conditions by adapting Eq. 5, as well as the resulting  $^{12}\text{C}/^{13}\text{C}$  isotopic ratio. For W3(OH), toward which the  $^{13}\text{CH}$  line remains undetected, we derive a  $2\sigma$  lower limit on the  $^{12}\text{CH}/^{13}\text{CH}$  abundance ratio of  $> 58$  over the velocity interval between  $(-55 - -38) \text{ km s}^{-1}$ .

The  $^{12}\text{C}/^{13}\text{C}$  isotopic abundance ratio has been determined towards the GC region using a wide variety of molecules ranging from simple species like  $\text{CO}$ ,  $\text{CN}$ ,  $\text{H}_2\text{CO}$  and  $\text{HCO}^+$  (Henkel et al. 1982; Langer & Penzias 1990; Savage et al. 2002) to more complex ones containing more than six atoms like  $\text{CH}_3\text{CH}_2\text{CN}$ ,

$\text{CH}_3\text{CCH}$ ,  $\text{CH}_2\text{CHCN}$  and  $\text{NH}_2\text{CHO}$  (Belloche et al. 2016; Halfen et al. 2017) to name a few. The relatively lower values of the  $^{12}\text{C}/^{13}\text{C}$  isotopic ratio towards the GC in comparison to the inner Galaxy, the local ISM and the solar system bears evidence to its advanced state of chemical evolution and reflects on its unique nucleosynthesis history. Moreover, the value of the GC strongly pivots the derived Galactic gradient. Therefore, as discussed by Halfen et al. (2017), it is essential to obtain more accurate measurements of the  $^{12}\text{C}/^{13}\text{C}$  ratio towards the GC region since several of the derived molecular isotopic ratios can be hindered by effects of optical depth and saturation, chemical fractionation and selective photo-dissociation. The limits on the  $^{12}\text{C}/^{13}\text{C}$  isotopic ratio derived using  $\text{CH}$  are consistent with those derived by Savage et al. (2002) using  $\text{CN}$  for our sample of sources except for G34.26+0.15. The latter difference could be due to difficulties in deriving the  $^{12}\text{CN}$  optical depth (meaning,

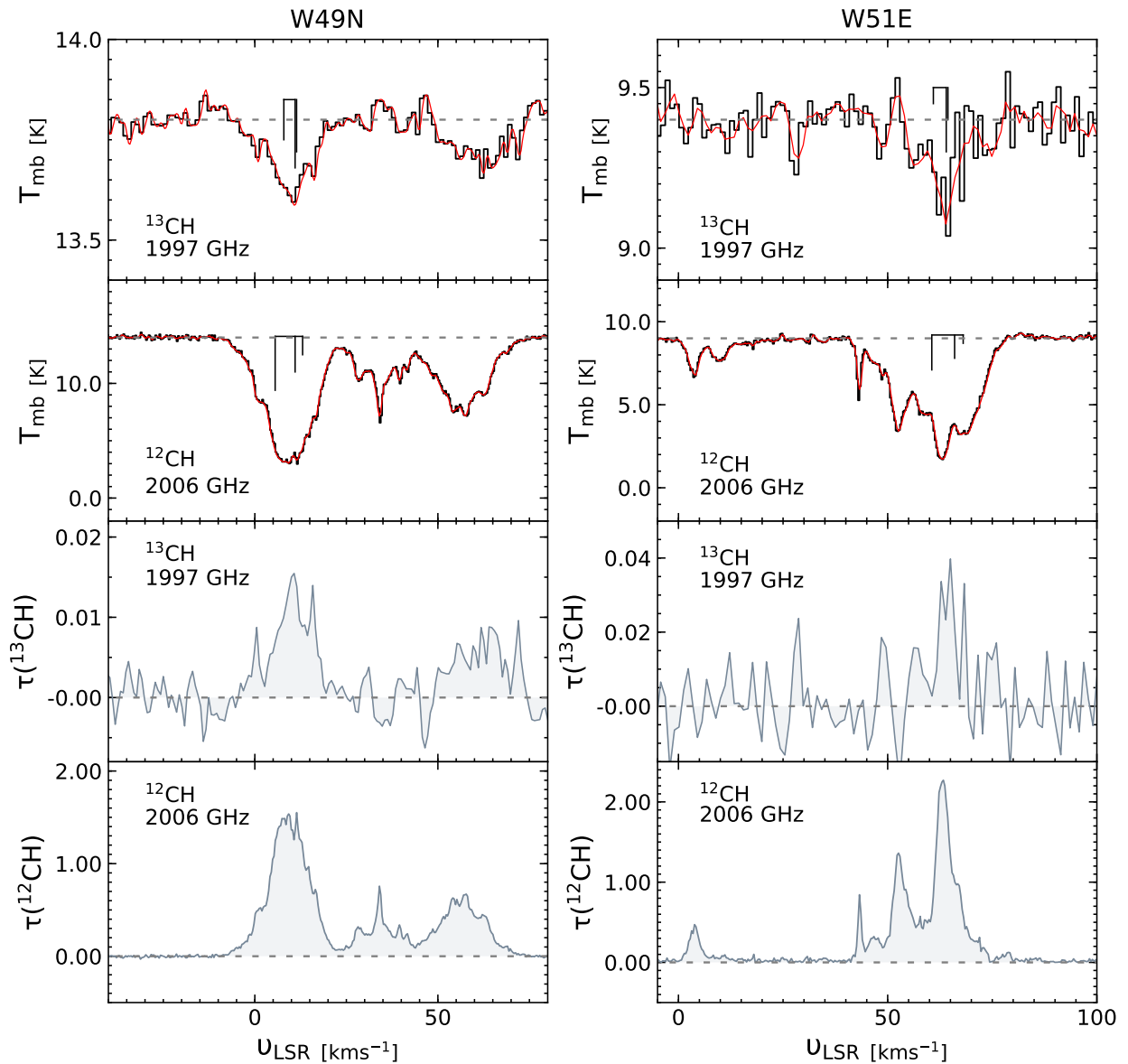


**Fig. 3.** Same as Fig. 2 but toward W49(N) (left) and W51E (right).

**Table 3.** Synopsis of the derived column densities and  $^{12}\text{C}/^{13}\text{C}$  isotopic ratios

Source	$u_{\min} - u_{\max}$ [km s $^{-1}$ ]	$N(^{13}\text{CH})$ [ $10^{13}$ cm $^{-2}$ ]	$N(^{12}\text{CH})$ [ $10^{13}$ cm $^{-2}$ ]	$^{12}\text{C}/^{13}\text{C}$	
				CH	CN <sup>a</sup>
Sgr B2(M)	40 – 90	$4.61^{+0.70}_{-0.71}$	$73.02^{+0.60}_{-0.68}$	$15.8^{+0.24}_{-0.24}$	>12
W51E	45 – 75	$1.77^{+0.20}_{-0.26}$	$66.36^{+3.30}_{-4.21}$	$37.5^{+0.61}_{-0.61}$	$35 \pm 12$
G34.26+0.15	35 – 70	$0.20^{+0.01}_{-0.02}$	$9.38^{+0.78}_{-0.93}$	$47.0^{+0.45}_{-0.66}$	$28 \pm 4$
W49(N)	-5 – 25	$0.68^{+0.11}_{-0.09}$	$22.87^{+3.56}_{-3.72}$	$33.6^{+0.75}_{-0.70}$	$44 \pm 22$
W3(OH)	-55 – -38	<0.11 <sup>b</sup>	$6.58^{+0.72}_{-1.35}$	>58	$63 \pm 16$

**Notes.** <sup>(a)</sup> Values taken from Milam et al. (2005) and references therein. <sup>(b)</sup> The column density for the non-detection was derived using the  $2\sigma$  rms of level.

an underestimation of the column density) because, as the authors of the above study state, the observed relative line intensity ratios of the hfs components does not follow LTE. The comparable isotopic compositions of the two molecular species

stems from their inter-linked formation routes<sup>8</sup> and suggests that CH similar to CN shows negligible amounts of fractionation.

<sup>8</sup> As the neutral-neutral reaction between CH and N forms one of the major formation pathways for the production of CN ( $\text{CH} + \text{N} \rightarrow \text{CN} + \text{H}$ ), with a forward reaction rate of  $\sim 6.7 \times 10^{-11}$  cm $^3$  s $^{-1}$  for a temperature of 50 K.

Further, Halfen et al. (2017) estimated  $^{12}\text{C}/^{13}\text{C}$  isotopic ratios between 19 and 33 using several different complex organic species and an average value of  $\sim 24 \pm 9$  towards the  $64 \text{ km s}^{-1}$  component of the GC source Sgr B2(N). Within the errors, the average  $^{12}\text{C}/^{13}\text{C}$  isotopic ratio derived by these authors is also consistent with the values derived from CH and CN. This presents solid evidence that the  $^{13}\text{C}$  isotopic enrichment in more complex molecules must arise from progenitor molecules like CH and CN since the  $^{13}\text{C}$  substitution of complex species via simple ion-molecule exchange reactions is not as straightforward as that of simple molecules.

In general, almost all the PDR models studied by Röllig & Ossenkopf (2013) with varying physical parameters display a  $^{12}\text{C}/^{13}\text{C}$  fractionation ratio that is enhanced at higher values of  $A_v$  ( $\geq 1$ ). The degree of fractionation is coupled with the FUV flux present in the models, the weaker the FUV flux, the greater is the fractionation ratio. The  $^{12}\text{C}/^{13}\text{C}$  isotopic ratios we derive from CH show no indication of an enhanced value in comparison to those derived from for e.g., CN as shown in Tab. 3 and therefore no signature of fractionation. This is because toward the SFRs toward which we detect both  $^{12}\text{C}/^{13}\text{C}$  and  $^{13}\text{C}$ , the absorption from both isotopologues primarily traces these regions' extended envelopes, which are exposed to a significant UV field and whose densities have been estimated to be of the order of  $10^3 \text{ cm}^{-3}$  on parsec scales for Sgr B2(M) and other regions (Schmiedeke et al. 2016; Wyrowski et al. 2016), a value typical for a translucent molecular cloud. The gas-phase carbon reservoir in such regions is predominantly in either its atomic or ionised form and not locked up in CO, which means that there is enough  $^{13}\text{C}$  and  $^{13}\text{C}^+$  present for ion-molecule exchange reactions to form  $^{13}\text{C}$ -substituted CH.

The previously determined  $^{12}\text{C}/^{13}\text{C}$  isotopic ratios suffer from large error bars that may either be due to opacity effects in the main isotopologue or other systematic effects. Therefore it is not clear whether the large dispersion in values between Galactocentric radii of 4 to 8 kpc, corresponding to regions with the most molecular mass content in the Milky Way (apart from the GC region), are due to actual cloud-cloud variations. If the spread is indeed due to opacity effects then the ground state rotational transitions of CH studied in this work which are free from such effects, should be well-suited to quantitatively constrain the  $^{12}\text{C}/^{13}\text{C}$  ratio. By combining the  $^{12}\text{C}/^{13}\text{C}$  ratio values derived using CH with those derived by Langer & Penzias (1990), Wouterloot & Brand (1996)<sup>9</sup>, Milam et al. (2005), Giannetti et al. (2014), Ritchey et al. (2011), and Halfen et al. (2017) and carrying out a weighted least squares fit, we derive a revised  $^{12}\text{C}/^{13}\text{C}$  Galactic gradient of  $^{12}\text{C}/^{13}\text{C} = 5.85(0.50) R_{\text{GC}} + 15.03(3.40)$ <sup>10</sup> displayed in Fig. 4. The addition of our CH data points plus those from Wouterloot & Brand (1996), Ritchey et al. (2011), and Giannetti et al. (2014) results in values for the best fit slope and intercept that are, within the combined uncertainties, consistent with the values derived by Halfen et al. (2017). The small uncertainties of the CH data result in somewhat smaller formal uncertainties of the fitted values.

<sup>9</sup> The authors of the cited article note that the discrepancy between the higher ratio derived from the  $J = 1 - 0$  lines of  $^{12}\text{C}^{18}\text{O}$  and  $^{13}\text{C}^{18}\text{O}$  to the lower value from the  $J = 2 - 1$  lines “is not yet explained, but may be due to the emission of the two transitions originating in different parts of the cloud with different excitation conditions.”

<sup>10</sup> The values in parentheses represent  $1\sigma$  uncertainties.

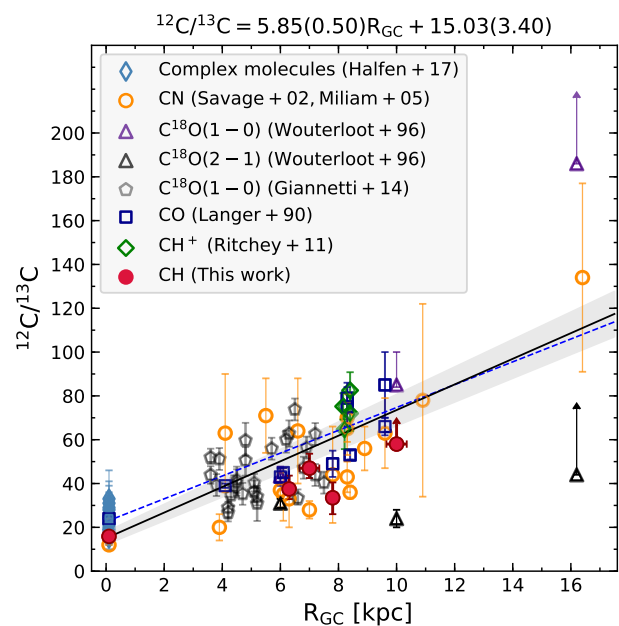


**Fig. 4.** Plot of  $^{12}\text{C}/^{13}\text{C}$  isotope ratios as a function of Galactocentric distance,  $R_{\text{GC}}$  (kpc). The filled red circles represent the  $^{12}\text{C}/^{13}\text{C}$  ratio obtained using CH (this paper) while the unfilled black and purple triangles, grey pentagons, yellow circles, dark blue squares and green, and light blue diamonds are those obtained using isotopologues of  $\text{C}^{18}\text{O}$  ( $J = 1 - 0$  and  $J = 2 - 1$  transitions) (Wouterloot & Brand 1996; Giannetti et al. 2014), CN (Savage et al. 2002; Milam et al. 2005), CO (Langer & Penzias 1990),  $\text{CH}^+$  (Ritchey et al. 2011), and complex organic molecules (Halfen et al. 2017), respectively. The black solid line represents the weighted fit to the data with the grey shaded region demarcating the  $1\sigma$  interval of this fit. For comparison the fit obtained by Halfen et al. (2017) is displayed by the dashed blue line.

## 5. Conclusions

In this paper we report the first detections of  $^{13}\text{CH}$  in the ISM, namely towards the Sgr B2(M), G34.26+0.15, W49(N), and W51E massive SFRs in the Milky Way. Hyperfine structure transitions connecting sub-levels of the  $^{13}\text{CH}$   $N, J = 2, 1/2$  and  $1, 1/2$   $\Lambda$ -doublet states with frequencies near 1997 GHz were observed in absorption using GREAT/SOFIA, which provides an avenue to observe frequency bands for which spectrally resolved observations were previously not possible with HIFI/Herschel or earlier missions. The detection of  $^{13}\text{CH}$  along with observations of the main isotopologue CH towards the same sources opens a new, independent way for determinations of the  $^{12}\text{C}/^{13}\text{C}$  isotopic abundance ratio across the Galaxy. We derive  $^{12}\text{C}/^{13}\text{C}$  isotopic ratios for those of our target sources with a  $^{13}\text{CH}$  detection and a lower limit for W3(OH) toward which we did not detect this isotopologue. Our values are in agreement with previous determinations made using varied chemical species and in particular CN. Our observations do not hint at a possible enhancement in the  $^{12}\text{C}/^{13}\text{C}$  ratio derived from CH as it traces the more diffuse and translucent regions of the ISM in which CO is not the main reservoir of carbon. Furthermore, as its abundance peaks in regions of high UV radiation, CH is relatively unaffected by selective photo-dissociation and optical depth effects like saturation. Hence, measurements of the  $^{12}\text{C}/^{13}\text{C}$  isotopic ratio based on the fundamental rotational lines of CH potentially reflect the actual  $^{12}\text{C}/^{13}\text{C}$  ratio in the gas.

In addition, knowledge of the  $^{13}\text{C}$  substitution in CH will improve our understanding of interstellar chemistry because



direct substitution of  $^{13}\text{C}$  in more complex species is currently poorly understood and their observed  $^{12/13}\text{C}$  isotopologue ratios are speculated to have their origin in simpler precursors like CH. Investigating a larger sample of SFRs at different Galactocentric radii for  $^{13}\text{CH}$  will allow for a better constraint on the average  $^{12}\text{C}/^{13}\text{C}$  abundance ratio value in the ISM and on the Galactic  $^{12}\text{C}/^{13}\text{C}$  gradient, facilitating accurate Galactic chemical evolution models. However, the requirement of very high signal-to-noise ratios at high spectral resolutions that are required to detect the weak  $^{13}\text{CH}$  absorption lines greatly restricts the selection of sources to those with strong continuum backgrounds for carrying out future, follow-up studies. Further, we hope that our study will encourage coordinated laboratory efforts resulting in refinements of the spectroscopic parameters of  $^{13}\text{CH}$ , for which, e.g., several of the constants describing the fine structure of its transitions have not yet been well established (Halfen et al. 2008)..

*Acknowledgements.* We would like to thank David Neufeld and the anonymous referee for their valuable comments which helped to improve the clarity of this paper. SOFIA Science Mission Operations is jointly operated by the Universities Space Research Association, Inc., under NASA contract NAS2-97001, and the Deutsches SOFIA Institut under DLR contract 50 OK 0901 and 50 OK 1301 to the University of Stuttgart. upGREAT is financed by resources from the participating institutes, and by the Deutsche Forschungsgemeinschaft (DFG) within the grant for the Collaborative Research Center 956, as well as by the Federal Ministry of Economics and Energy (BMWi) via the German Space Agency (DLR) under Grants 50 OK 1102, 50 OK 1103 and 50 OK 1104. We are GREATful to the SOFIA operations team for their help and support throughout the course of the observations and after. The authors would like to express our gratitude to the developers of the many C++ and Python libraries, made available as open-source software, in particular this research has made use of the NumPy (van der Walt et al. 2011), SciPy (Jones et al. 2001) and matplotlib (Hunter 2007) packages.

## References

- Bally, J. & Langer, W. 1982, *The Astrophysical Journal*, 255, 143  
 Belloche, A., Müller, H. S. P., Garrod, R. T., & Menten, K. M. 2016, *A&A*, 587, A91  
 Bergin, E. A., Phillips, T. G., Comito, C., et al. 2010, *A&A*, 521, L20  
 Bottinelli, S., Wakelam, V., Caux, E., et al. 2014, *MNRAS*, 441, 1964  
 Dagdigan, P. J. 2018, *MNRAS*, 475, 5480  
 Danks, A. C., Federman, S. R., & Lambert, D. L. 1984, *A&A*, 130, 62  
 Davidson, S. A., Evenson, K. M., & Brown, J. M. 2004, *Journal of Molecular Spectroscopy*, 223, 20  
 Dunham, T. 1937, *Publications of the Astronomical Society of the Pacific*, 49, 26  
 Falgarone, E., Godard, B., Cernicharo, J., et al. 2010, *A&A*, 521, L15  
 Federman, S. R. 1982, *ApJ*, 257, 125  
 Gerin, M., de Luca, M., Goicoechea, J. R., et al. 2010, *A&A*, 521, L16  
 Giannetti, A., Wyrowski, F., Brand, J., et al. 2014, *A&A*, 570, A65  
 Godard, B., Falgarone, E., Gerin, M., et al. 2012, *A&A*, 540, A87  
 Godard, B., Falgarone, E., & Pineau des Forêts, G. 2014, *A&A*, 570, A27  
 Guan, X., Stutzki, J., Graf, U. U., et al. 2012, *A&A*, 542, L4  
 Halfen, D. T., Woolf, N. J., & Ziurys, L. M. 2017, *ApJ*, 845, 158  
 Halfen, D. T., Ziurys, L. M., Pearson, J. C., & Drouin, B. J. 2008, *ApJ*, 687, 731  
 Henkel, C., Wilson, T. L., & Bieging, J. 1982, *A&A*, 109, 344  
 Henkel, C., Wilson, T. L., Langer, N., Chin, Y. N., & Mauersberger, R. 1994, *Interstellar CNO Isotope Ratios*, Vol. 439 (Springer), 72–88  
 Herwig, F. 2005, *Annu. Rev. Astron. Astrophys.*, 43, 435  
 Hierl, P. M., Morris, R. A., & Viggiano, A. A. 1997, *J. Chem. Phys.*, 106, 10145  
 Hunter, J. D. 2007, *Computing in Science Engineering*, 9, 90  
 Jacob, A. M., Menten, K. M., Wiesemeyer, H., et al. 2019, *A&A*, 632, A60  
 Jones, E., Oliphant, T., Peterson, P., et al. 2001, *SciPy: Open source scientific tools for Python*  
 Kester, D., Higgins, R., & Teyssier, D. 2017, *A&A*, 599, A115  
 Klein, B., Hochgürtel, S., Krämer, I., et al. 2012, *A&A*, 542, L3  
 Langer, W. D. & Penzias, A. A. 1990, *The Astrophysical Journal*, 357, 477  
 Milam, S., Savage, C., Brewster, M., Ziurys, L. M., & Wyckoff, S. 2005, *The Astrophysical Journal*, 634, 1126  
 Neill, J. L., Bergin, E. A., Lis, D. C., et al. 2014, *ApJ*, 789, 8  
 Neufeld, D. A., Godard, B., Gerin, M., et al. 2015, *A&A*, 577, A49

- Neufeld, D. A., Zmuidzinas, J., Schilke, P., & Phillips, T. G. 1997, *ApJ*, 488, L141  
 Ossenkopf, V., Röllig, M., Neufeld, D. A., et al. 2013, *A&A*, 550, A57  
 Pagel, B. 1997, *Nucleosynthesis and Chemical Evolution of Galaxies*, Cambridge Univ  
 Pickett, H., Poynter, R., Cohen, E., et al. 1998, *J. Quant. Spec. Radiat. Transf.*, 60, 883  
 Prantzos, N., Aubert, O., & Audouze, J. 1996, *A&A*, 309, 760  
 Qin, S.-L., Schilke, P., Comito, C., et al. 2010, *A&A*, 521, L14  
 Reid, M. J., Menten, K. M., Brunthaler, A., et al. 2014, *ApJ*, 783, 130  
 Richter, J. & Tonner, K.-F. 1967, *Zeitschrift für Astrophysik*, 67, 155  
 Risacher, C., Güsten, R., Stutzki, J., et al. 2016, *A&A*, 595, A34  
 Ritchey, A. M., Federman, S. R., & Lambert, D. L. 2011, *ApJ*, 728, 36  
 Röllig, M., & Ossenkopf, V. 2013, *Astronomy & Astrophysics*, 550, A96  
 Roueff, E., Loison, J. C., & Hickson, K. M. 2015, *A&A*, 576, A99  
 Rydbeck, O. E. H., Elldér, J., & Irvine, W. M. 1973, *Nature*, 246, 466  
 Sato, M., Reid, M. J., Brunthaler, A., & Menten, K. M. 2010, *ApJ*, 720, 1055  
 Savage, C., Apponi, A. J., Ziurys, L. M., & Wyckoff, S. 2002, *ApJ*, 578, 211  
 Schmiedeke, A., Schilke, P., Möller, T., et al. 2016, *A&A*, 588, A143  
 Sheffer, Y., Rogers, M., Federman, S. R., et al. 2008, *ApJ*, 687, 1075  
 Stacey, G. J., Lugten, J. B., & Genzel, R. 1987, *ApJ*, 313, 859  
 Steimle, T. C., Woodward, D. R., & Brown, J. M. 1986, *J. Chem. Phys.*, 85, 1276  
 Swings, P. & Rosenfeld, L. 1937, *ApJ*, 86, 483  
 Tang, X. D., Henkel, C., Menten, K. M., et al. 2019, *A&A*, 629, A6  
 Tieftrunk, A., Pineau des Forêts, G., Schilke, P., & Walmsley, C. M. 1994, *A&A*, 289, 579  
 Tosi, M. 1982, *The Astrophysical Journal*, 254, 699  
 van der Walt, S., Colbert, S. C., & Varoquaux, G. 2011, *Computing in Science Engineering*, 13, 22  
 Watson, J. K. 2001, *The Astrophysical Journal*, 555, 472  
 Wiesemeyer, H., Güsten, R., Menten, K. M., et al. 2018, *A&A*, 612, A37  
 Wilson, T. 1999, *Reports on Progress in Physics*, 62, 143  
 Wilson, T. L. & Rood, R. 1994, *ARA&A*, 32, 191  
 Wouterloot, J. G. A. & Brand, J. 1996, *A&AS*, 119, 439  
 Wyrowski, F., Güsten, R., Menten, K. M., et al. 2016, *A&A*, 585, A149  
 Xu, Y., Reid, M. J., Zheng, X. W., & Menten, K. M. 2006, *Science*, 311, 54  
 Young, E. T., Becklin, E. E., Marcum, P. M., et al. 2012, *ApJ*, 749, L17  
 Zhang, B., Reid, M. J., Menten, K. M., et al. 2013, *ApJ*, 775, 79  
 Zhang, B., Zheng, X. W., Reid, M. J., et al. 2009, *ApJ*, 693, 419

## Appendix A: Sideband deconvolution

In Fig. A.1 we display the  $^{13}\text{CH}$  spectra toward Sgr B2(M) obtained from the different IF settings at 1.4, 1.6, and 1.8 GHz, respectively. The secondary x-axis displayed in each panel showcases the velocity scale in the image band LSR. Note that each IF offset of 0.2 GHz corresponds to a shift of the image band features by  $60 \text{ km s}^{-1}$ . When using an IF setting of 1.4 GHz, both sets of  $\Lambda$ -doublet features are well separated, with the hyperfine components corresponding to the 1997 GHz doublet originating from the signal band while those corresponding to the 2001 GHz doublet arise from the image band. The  $^{13}\text{CH}$  (signal band)  $\Lambda$ -doublet are seen in absorption with a deeper absorption feature seen at 1996.589 GHz possibly arising from the  $J_{K^-,K^+} = 4_{3,2} \rightarrow 3_{2,1}$  transitions of  $\text{H}_2\text{S}$ . Several transitions of  $\text{H}_2\text{S}$  have previously been detected towards the Sgr B2(M) (Tieftrunk et al. 1994) and Sgr B2(N) (Neill et al. 2014) SFRs, with the higher frequency transitions typically seen in absorption towards the envelope of these hot-cores. This transition lying close to 1996 GHz was not previously detected using HIFI/Herschel since it lies outside the tuning range of HIFI Band 7. However, the  $J_{K^-,K^+} = 6_{1,6} \rightarrow 5_{0,5}$  high-energy transition of  $\text{H}_2\text{S}$  at 1846.76 GHz with a lower level energy  $\sim 239 \text{ K}$  was observed using HIFI/Herschel toward Sgr B2(M) as a part of the HEXOS guaranteed time key programme<sup>11</sup> with observation id 1342206640 showcases a similar absorption profile with comparable line-widths and peak temperatures,

<sup>11</sup> HIFI/Herschel observations of EXtra-Ordinary Sources (HEXOS) (Bergin et al. 2010) was aimed to investigate the chemical composition of several sources in the Orion and Sgr B2 SFRs.

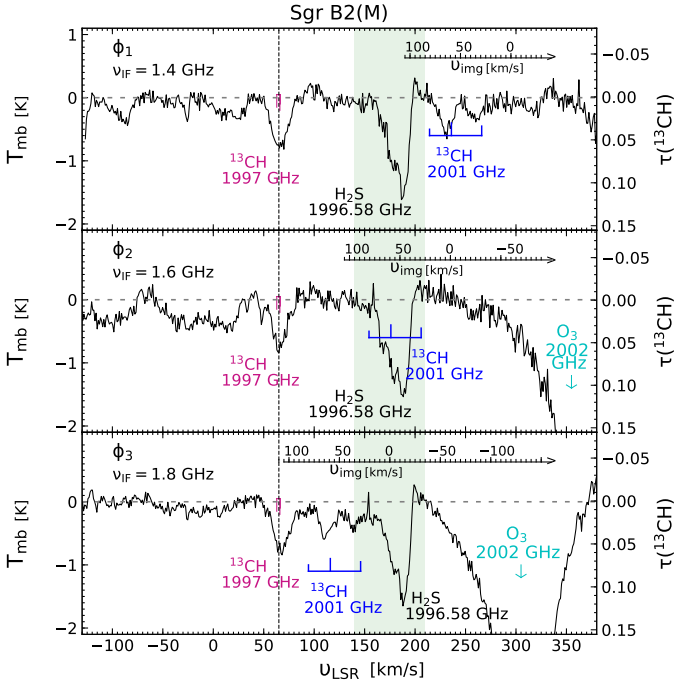


**Fig. A.1.** Calibrated and baseline-subtracted observed  $^{13}\text{CH}$  spectra at an IF setting of 1.4 GHz (top panel), 1.6 GHz (central panel), and 1.8 GHz (bottom panel) toward Sgr B2(M). The secondary y-axis in each panel presents the optical depth scale. Signal bandpass contamination, possibly from the  $J_{K^-K^+} = 4_{3,2} \rightarrow 3_{2,1}$  transitions of  $\text{H}_2\text{S}$  at 1996.589 GHz is displayed by the green shaded region. The hyperfine transitions corresponding to the 1997 GHz  $\Lambda$ -doublet arising from the signal band are displayed in pink while that of the 2001 GHz  $\Lambda$ -doublet arising from the image band are displayed in blue. The change in IF pushes both the second  $\Lambda$ -doublet as well as the atmospheric ozone feature at 2002.347 GHz (telluric rest frame, marked in cyan) towards the signal band features. The secondary x-axis in each panel represents the image band LSR velocity scale.

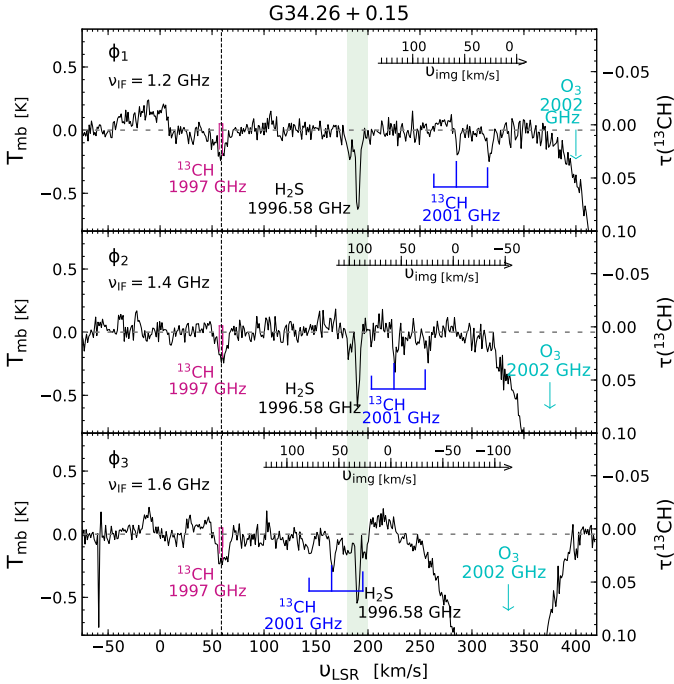


**Fig. A.2.** Same as Fig. A.1, but toward G34.26+0.15 for IF settings of 1.2, 1.4, and 1.6 GHz (from top to bottom).

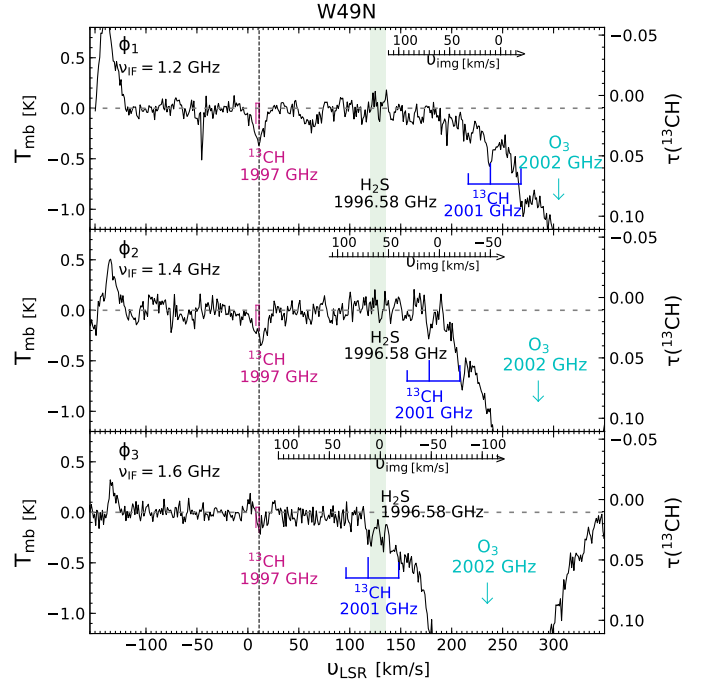


**Fig. A.3.** Same as Fig. A.1, but toward W49(N) for IF settings of 1.2, 1.4, and 1.6 GHz (from top to bottom).

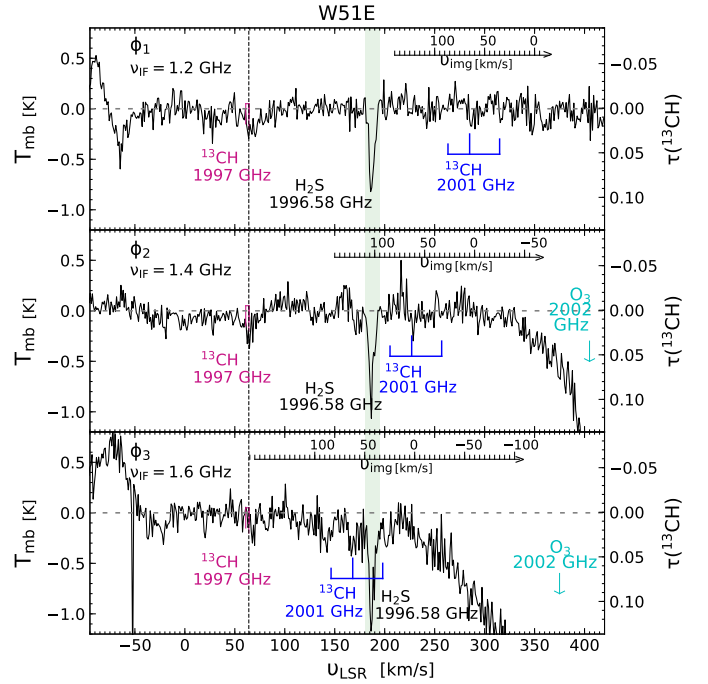


**Fig. A.4.** Same as Fig. A.1, but toward W51E for IF settings of 1.2, 1.4, and 1.6 GHz (from top to bottom).

which further validates our assumption of this line arising from  $\text{H}_2\text{S}$ .

Despite pushing the 2001 GHz  $\Lambda$ -doublet transitions into the atmospheric ozone feature at 2002.347 GHz, the additional observing setup with an IF of 1.6 GHz was used to confirm the origin of the deeper absorption feature as being from the signal band. Using this setup it is clear that the deeper  $\text{H}_2\text{S}$  absorption feature must arise from the signal band while further confirming our detection of  $^{13}\text{CH}$  absorption toward the

envelope of the SFR. However, we require a third IF setting in order to confirm the presence of weak sight-line absorption features. When increasing the IF offset to 1.8 GHz, the  $^{13}\text{CH}$  features arising from the image band move closer towards the  $^{13}\text{CH}$  features arising from the signal band. We compare the average of the residuals between two independent IF settings with the average of the IF co-added spectrum. Whilst affirming the presence of weaker LOS absorption features by suppressing the image band contributions, this does not present a complete DSB deconvolution. This can be mathematically formulated as follows:

Representing the DSB  $^{13}\text{CH}$  spectrum obtained from each IF setting as a function of velocity as,

$$\phi(\nu)_i = \phi_{\text{sig}}(\nu) + \phi_{\text{img}}(\nu_i - \nu), \quad (\text{A.1})$$

where,  $i = 1, 2, 3$  corresponding to the different IF settings at 1.4, 1.6, and 1.8 GHz, respectively,  $\nu_i$  is the signal-band velocity at which the image-band velocity is equal to zero and  $\phi_{\text{sig}}$ , and  $\phi_{\text{img}}$  represent the signal, and image band contributions. From Eq. A.1 the average of the IF co-added spectrum is,

$$\phi(\nu)_{\text{avg}} = \phi_{\text{sig}}(\nu) + \frac{1}{3} \left( \phi_{\text{img}}(\nu_1 - \nu) + \phi_{\text{img}}(\nu_2 - \nu) + \phi_{\text{img}}(\nu_3 - \nu) \right), \quad (\text{A.2})$$

The set of independent residuals between the different IF settings using the spectrum with an IF = 1.4 GHz as reference is,

$$\phi(\nu)_{1-2} = \phi(\nu)_1 - \phi(\nu)_2, \quad (\text{A.3})$$

$$\phi(\nu)_{1-3} = \phi(\nu)_1 - \phi(\nu)_3. \quad (\text{A.4})$$

The average of these residuals will reduce the image band features from the spectra with IF settings 1.6 and 1.8 GHz by half.

$$\phi_{\text{residual-avg}} = (\phi(\nu)_{1-2} + \phi(\nu)_{1-3}) / 2 \quad (\text{A.5})$$

$$= \left( 2\phi_{\text{img}}(\nu_1 - \nu) - \phi_{\text{img}}(\nu_2 - \nu) - \phi_{\text{img}}(\nu_3 - \nu) \right) / 2 \quad (\text{A.6})$$

Subtracting Eq. A.6 from Eq. A.2 yields,

$$\phi_{\text{resultant}} = \phi_{\text{avg}} - \phi_{\text{residual-avg}} \quad (\text{A.7})$$

$$= \phi_{\text{sig}}(\nu) - \frac{2}{3}\phi_{\text{img}}(\nu_1 - \nu) + \frac{5}{6}\phi_{\text{img}}(\nu_2 - \nu) + \frac{5}{6}\phi_{\text{img}}(\nu_3 - \nu) \quad (\text{A.8})$$

While this exercise models the contribution of the 2001 GHz transitions of  $^{13}\text{CH}$ , it does not confirm the profiles of the LOS features. Additionally, discrepancies in the noise level between the three spectral tunings arising from different integration times between them may lead to errors in the sideband reconstruction. However, the detection of  $^{13}\text{CH}$ , at the systemic velocity of the Sgr B2(M) molecular cloud, remains undeterred.

A similar DSB deconvolution was carried out for G34.26+0.15, W49(N) and W51E using a nominal IF setting of 1.2, 1.2, and 1.4 GHz, respectively as reference. The spectra observed using each of the three different IF tunings toward each of these sources are displayed in Figures A.2, A.3 and A.4, respectively. We clearly detect the  $^{13}\text{CH}$  1997 GHz  $\Lambda$ -doublet component at the respective systemic velocities of G34.26+015, W49(N), and W51E, in all three IF settings at 1.2, 1.4 and

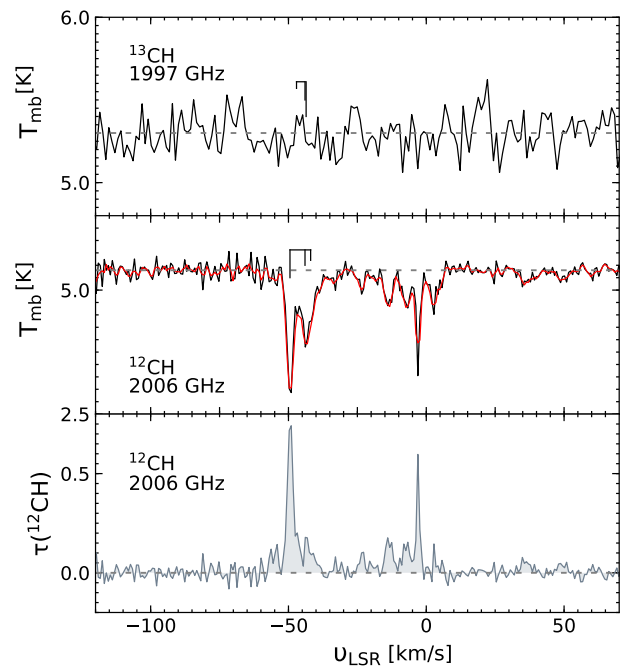


**Fig. B.1.** Spectra of the  $N, J = 2, 3/2 \rightarrow 1, 1/2$  transitions of  $^{13}\text{CH}$  near 1997 GHz (top) and CH near 2006 GHz (middle) observed towards W3(OH) in black. The Wiener filter model of the observed CH spectrum is overlaid in red. The bottom panel presents the Wiener filter deconvolved CH spectrum in optical depth scales.

1.6 GHz, however the hyperfine lines of the 2001 GHz  $\Lambda$ -doublet component either lie at the edge of the ozone feature for an IF setting of 1.2 GHz or move into the  $\text{H}_2\text{S}$  absorption feature for the higher IF tuning at 1.6 GHz. Despite, confirming the detection of  $^{13}\text{CH}$  toward the systemic velocities of these sources, it is once again difficult to establish the presence of any LOS features post the sideband deconvolution.

## Appendix B: $^{13}\text{CH}$ spectrum toward W3(OH)

In this Appendix we display the  $^{13}\text{CH}$  spectrum toward W3(OH).